

Creating superconductivity in WB_2 through pressure-induced metastable planar defects

Received: 5 October 2021

Accepted: 18 November 2022

Published online: 22 December 2022



J. Lim^{1,7}, A. C. Hire^{2,3,7}, Y. Quan^{1,2,3}, J. S. Kim¹, S. R. Xie^{2,3}, S. Sinha¹,
R. S. Kumar⁴, D. Popov⁵, C. Park⁵, R. J. Hemley⁴, Y. K. Vohra⁶,
J. J. Hamlin¹✉, R. G. Hennig^{2,3}, P. J. Hirschfeld¹ & G. R. Stewart¹

High-pressure electrical resistivity measurements reveal that the mechanical deformation of ultra-hard WB_2 during compression induces superconductivity above 50 GPa with a maximum superconducting critical temperature, T_c of 17 K at 91 GPa. Upon further compression up to 187 GPa, the T_c gradually decreases. Theoretical calculations show that electron-phonon mediated superconductivity originates from the formation of metastable stacking faults and twin boundaries that exhibit a local structure resembling MgB_2 (hP3, space group 191, prototype AlB_2). Synchrotron x-ray diffraction measurements up to 145 GPa show that the ambient pressure hP12 structure (space group 194, prototype WB_2) continues to persist to this pressure, consistent with the formation of the planar defects above 50 GPa. The abrupt appearance of superconductivity under pressure does not coincide with a structural transition but instead with the formation and percolation of mechanically-induced stacking faults and twin boundaries. The results identify an alternate route for designing superconducting materials.

In 2001, superconductivity with a remarkably high critical temperature of 39 K was discovered in MgB_2 . Efforts to increase T_c beyond the ambient pressure value in the material invariably proved unsuccessful, as both pressure^{1,2} and various chemical substitutions^{3,4} caused a decrease in the critical temperature. After two decades of searching for further high- T_c superconductors in the diboride family of compounds, Pei et al.⁵ recently discovered that MoB_2 transforms from the hR6, ($R\bar{3}m$, $CaSi_2$) structure to the hP3 ($P6/mmm$, AlB_2 or MgB_2) structure above 70 GPa, and exhibits a T_c that reaches 32 K at 100 GPa.

Inspired by this result, we have synthesized single crystals of the isolectronic compound WB_2 , which forms at ambient pressure in the hP12 ($P6_3/mmc$) structure. Investigating this compound in a series of experiments to pressures as high as 187 GPa, we discovered that WB_2 becomes superconducting near 50 GPa, with T_c jumping rapidly to about 17 K and varying weakly with pressure thereafter.

Interestingly, WB_2 had been studied earlier at ambient pressure, with results that differ from ours. A critical temperature of $T_c = 5.4$ K was reported in ref. 6, along with extensive X-ray and neutron diffraction data, leading to a suggestion that the hP12 structure was realized in large-grain polycrystalline samples. This work emphasized that WB_2 had previously been identified as W_2B_5 ⁷. The reason for the difficulty of extracting the correct structure in diffraction patterns is the enormous Z -contrast between W (74) and B (5), such that the B positions are difficult to ascertain. Therefore, theoretical studies are needed to resolve the origin of the reported ambient pressure superconductivity, the difference with our results, and the jump of T_c to 17 K at 91 GPa. By themselves, our resistivity data might suggest a transition to a new structure. However, synchrotron X-ray diffraction measurements under pressure indicate that the material, or a major part of it, retains the

¹Department of Physics, University of Florida, Gainesville, FL 32611, USA. ²Department of Materials Science and Engineering, University of Florida, Gainesville, FL 32611, USA. ³Quantum Theory Project, University of Florida, Gainesville, FL 32611, USA. ⁴Department of Physics, Chemistry, and Earth and Environmental Sciences, University of Illinois Chicago, Chicago, IL 60607, USA. ⁵HPCAT, X-ray Science Division, Argonne National Laboratory, Argonne, IL 60439, USA.

⁶Department of Physics, University of Alabama at Birmingham, Birmingham, AL 35294, USA. ⁷These authors contributed equally: J. Lim, A. C. Hire.

✉ e-mail: jhamlin@ufl.edu

ambient pressure hP12 structure with a monotonically increasing c/a ratio. Given the weak scattering of X-rays by B, small contributions from hR6 and hP3 may be present.

To explain the experimental observations, we explored the relative stability of relevant phases and investigated their superconducting properties as a function of pressure using density-functional theory (DFT). The ambient pressure hP12 phase is found to have nearly the lowest enthalpy up to pressures of 120 GPa, whereas the MgB₂-like hP3 phase is strongly disfavored over most of this range. However, the hP12 phase was calculated to have a very low critical temperature ($T_c < 1$ K) over these pressures. On the other hand, the metastable hP3 phase is predicted to have a critical temperature of 25–40 K over a wide pressure range. Thus, while the hP3 structure might explain the finding of higher T_c , it is never sufficiently stable.

To resolve this paradox, we have investigated defect structures intermediate between the hP3 and hP12 phases, i.e., those involving twin boundaries and stacking faults. Based on their formation enthalpies, we estimate that such planar defects plausibly occur within the hP12 phase during plastic deformation of the sample. These defect structures resemble nanometer-thick regions of the hP3 and hR6 structures, with W atoms in eclipsing positions above and below unbuckled B hexagons. We thus argue that the observed superconductivity appears following the formation of significant quantities of stacking faults above 50 GPa, which percolate through the sample above 100 GPa. In contrast to our results obtained on single crystals, the presence of hR6-like planar defects may also explain the

superconductivity observed at ambient pressure in large-grain polycrystalline samples⁶.

This unprecedented creation of superconductivity through mechanically induced metastable defects opens opportunities to search for other materials systems where metastable structures can be stabilized in the form of planar defects. While interfaces and twin boundaries can lead to surface phonons that somewhat increase an existing T_c ⁸, the mechanism here involves the formation of percolating metastable planar defects induced by mechanical processing, thereby inducing superconductivity. This offers the potential to stabilize at ambient pressure defect microstructures that exhibit novel properties. With the discovery of high- T_c superconductivity in high-pressure hydrides^{9,10}, new routes are being sought to stabilize metastable high- T_c superconductivity¹¹, and our proposal may represent a promising direction toward this goal.

Results

Experiment

We synthesized high-quality single crystals of WB₂ using an arc-melting technique described in the Methods section. Figure 1 presents a summary of the electrical resistivity measurements on one of these samples, extending from 1.8 to 297 K and to pressures as high as 187 GPa. The pressure values shown are measured at 10 K. The residual-resistivity ratio (RRR) at 6 GPa is 2.24 calculated from $\rho(297\text{ K}) = 0.118\text{ m}\Omega\text{-cm}$ over $\rho(1.8\text{ K}) = 0.053\text{ m}\Omega\text{-cm}$. Superconductivity first appears at 57 GPa as a broad, incomplete drop in the resistivity, with an onset near 4 K (Fig. 1a)

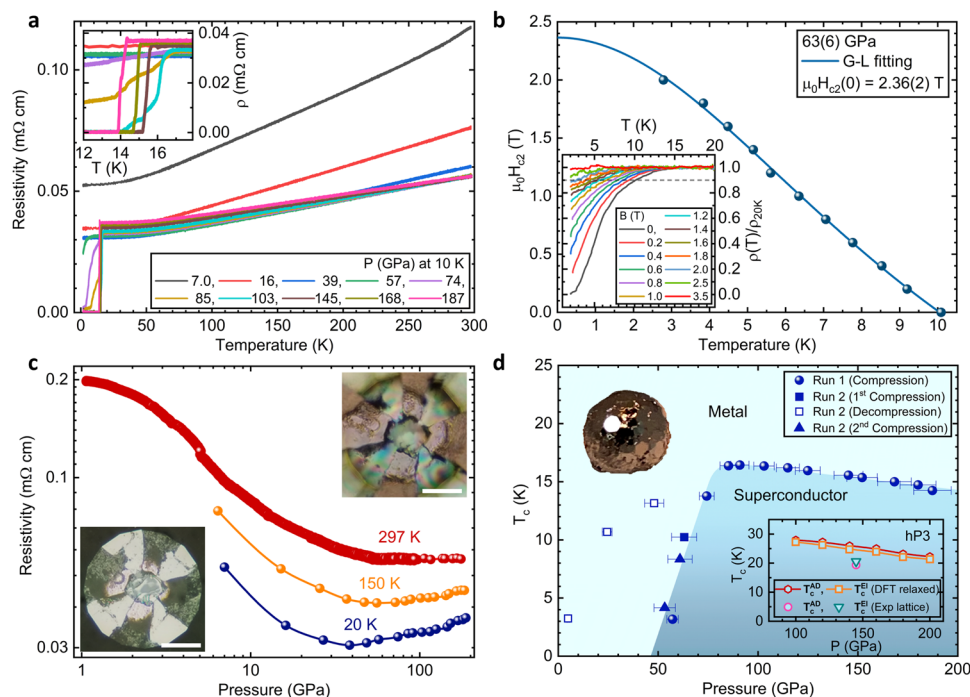


Fig. 1 | Representative high-pressure resistivity curves and $T_c(P)$ phase diagram. **a** Temperature-dependent resistivity curves of WB₂ measured while warming at several pressures to 187 GPa during compression (7.0 and 16 GPa data measured while cooling). The reported pressures are measured at 10 K. The black crossed lines represent the criterion used to determine T_c (onset). The inset shows an enlarged view of the superconducting transition. **b** Temperature-dependent upper critical field of WB₂ at 63 GPa (Run 2). The dark cyan solid line refers to Ginzburg–Landau (G-L) fitting. The inset shows temperature-dependent relative resistivity curves (after smoothing) under different magnetic fields to 3.5 T. The gray dashed line indicates 90% of the normal-state value, where the T_c is defined for the upper critical field. **c** Pressure-dependent resistivity curves at room temperature (RT), 150, and 20 K. The insets show photographs of the experimental setup at -1 (lower left) and 173 GPa (upper right), respectively. The white scale bars indicate

50 μm . **d** Superconducting phase diagram of WB₂ with pressure (at 10 K) using the 90% criterion. Closed dark blue symbols (spheres, a square, and triangles) indicate the T_c taken from compression (Run 1 and Run 2), whereas open blue square symbols are from decompression (Run 2). A sharp increase of T_c is present around 70 GPa. The inset in the upper left shows a photograph of an arc-melted boule of WB₂. Hexagonal crystal facets are visible on the surface. A small single crystalline fragment of the larger boule was selected for the electrical resistivity measurements under pressure. A second inset at lower right shows the Eliashberg theory T_c calculated for WB₂ in the hP3 structure with DFT relaxed lattice constants at 100, 120, 140, 160, and 180 GPa (orange squares), along with the Allen–Dynes T_c (red hexagons). A magenta circle and a green upside-down triangle show similar calculations for experimental lattice constants at 145 GPa.

marked by two crossing lines for T_c (onset). With further pressure increase, T_c goes up rapidly at a rate of 0.72 K/GPa. At 74 GPa, the transition onset has reached 17 K, but the transition remains broad, with the resistance failing to reach zero at the lowest temperatures. Additional pressure increases have only a weak effect on the superconducting transition onset temperature with a rate of -0.024 K/GPa, but the transition becomes much sharper. Zero resistance is achieved for pressures above 80 GPa. The superconductivity of WB_2 is further supported by the suppression of T_c with increasing external magnetic fields as shown in Fig. 1b. The temperature-dependent relative resistivity curves at 63 GPa in Fig. 1b inset show that the superconducting transition is suppressed by increasing field and completely destroyed above 3.5 T, where T_c is defined as the temperature at which the resistance has dropped to 90% of the normal-state resistivity just above the transition. The temperature-dependent upper critical fields are fitted using the empirical Ginzburg–Landau (G-L) formula, $\mu_0 H_{c2}(T) = \mu_0 H_{c2}(0)(1 - t^2)/(1 + t^2)$, where t is the temperature normalized to the zero-field superconducting transition temperature T/T_{c0} and $\mu_0 H_{c2}(0)$ is the zero-temperature upper critical field. The G-L fitting provides 2.36 T for $\mu_0 H_{c2}(0)$ at 63 GPa. Figure 1c shows the electrical resistivity as a function of pressure at three different temperatures. The room temperature resistivity drops monotonically, but at the lowest temperatures (20 K) the resistivity, which is related to the residual resistivity due to the defect scattering, exhibits a broad minimum as a function of pressure. This minimum appears to roughly coincide with the pressure at which superconductivity first appears above 50 GPa.

The pressure dependence of T_c is shown in Fig. 1d using the 90% criterion. Below 50 GPa, no trace of superconductivity is observed down to 1.8 K. Superconductivity suddenly appears above 50 GPa, with T_c rapidly rising to 14 K. On subsequent pressure increase, the transition temperature passes through a broad maximum with a maximum of 17 K (onset) near 90 GPa and then gradually declines. The broad superconducting transitions in the pressure range between 50 and 90 GPa, together with the sudden increase in the onset temperature in this range, suggests that the transition temperature in fact increases discontinuously, and that the broad resistive transitions may be caused by incomplete percolation of the superconducting phase through the sample. We note that broad, multi-step transitions have been observed in other systems in the vicinity of transitions between different structural/electronic phases¹². The pressure-dependent superconducting transition temperature is shown to be reproducible in Run 2 (see also Supplementary Fig. 7) under compression to 63 GPa. Interestingly, under decompression to 48 GPa, T_c first increases from -10 to 13 K and then decreases to with further decompression to 4.9 GPa. This irreversible behavior suggests the superconducting phase of WB_2 is metastable at low pressure. The subsequent second compression on the same sample in Run 2 after completely opening the cell and released to ambient pressure, the superconductivity reappears only above 50 GPa (See Supplementary Fig. 8 and Fig. 1d), consistent with the compression behavior in Run 1. These additional results suggest that the planar defects and twin boundaries responsible for superconductivity are only (meta)stable under high pressure. The abrupt appearance of superconductivity with a large $T_c(P)$ slope, followed by a sudden change to a lower slope at higher pressures is suggestive of a possible structural transition. However, the normal-state electrical resistivity does not exhibit any clear features that could be attributed to a structural transition. We carried out high-pressure X-ray diffraction measurements in order to determine if a structural transition could be responsible for the appearance of superconductivity.

Figure 2 summarizes the X-ray diffraction data that we have obtained on WB_2 to pressures as high as 145 GPa using Ne as the quasi-hydrostatic pressure medium. The diffraction patterns in Fig. 2a (Run 1) and b (Run 2) used different X-ray wavelengths (0.41 and 0.31 Å, respectively), and present a consistent result. The patterns are well described by the ambient pressure hP12 structure ($P6_3/mmc$, 194)¹³.

Figure 2c shows the experimental unit-cell volume along with the theoretically obtained results relaxed using PBEsol and PBE functional for the DFT calculations. The theoretically calculated volumes agree well with the experimental values, with a slight overestimation in the DFT calculated volumes, as expected¹⁴. The obtained bulk modulus (B_0) 267 GPa from a Vinet equation of state fit is relatively low compared to a previous experimental study finding 349 GPa from ambient pressure ultrasonic measurements¹⁵.

Figure 2d, e shows the comparison of experimental XRD patterns for WB_2 at 2.3 and 145 GPa, respectively, with the five different structure models calculated and shown in Fig. 3. The hP12 structure, which is found to be the ambient structure¹³, is still the most probable structure for bulk high-pressure phase to 145 GPa as the peak positions best line up with the experimental XRD patterns. The extra peaks in Fig. 2e, which are marked by the red and black asterisk symbols, come from the Ne pressure medium and Re gasket, respectively. To account for the effects of stress and strain in WB_2 under nonhydrostatic pressure condition similar to the electrical resistivity measurements, we have performed XRD measurements up to 98 GPa without any pressure medium filling the Re gasket hole with only the WB_2 sample (see Supplementary Fig. 9). The results indicate mostly hP12 phase except for one or two peaks appearing above 50 GPa that may be due to hP3 or hR6 phase as the possible local defects. Therefore, it is concluded that there is no bulk structural transition to hP3 or hR6 structure and WB_2 remains predominantly in the hP12 phase even in nonhydrostatic pressure condition in agreement with the quasi-hydrostatic XRD measurements in Fig. 2. Figure 2f shows the crystal structures of five competing phases of WB_2 from ref. 12. Out of these five competing phases, the tI12 phase forms a 3-d network structure. The remaining four competing phases form a layered structure, where the boron layers are either buckled or unbuckled depending on the position of the tungsten atoms in between the layers.

Theory of bulk phases

Figure 3 shows the calculated enthalpy as a function of pressure for various competing phases of WB_2 . According to our calculations, the WB_2 hP6 structure has (by a small margin) the lowest enthalpy at ambient pressure conditions but is not observed in the experimental sample. The theoretical enthalpy of the experimentally observed hP12 structure is about -16 meV/atom higher than the hP6 structure. We used arc melting to synthesize the samples, which were then quickly cooled to room temperatures on a water cooled Cu hearth. At the arc-melting temperatures (~ 2370 K), entropic contributions to the Gibbs free energy can easily overcome the energy difference of 16 meV/atom between the hP12 and hP6 phases. And because of the quick cooling of the samples, the high-temperature metastable hP12 phase, as is evident from the XRD, is retained at room temperature. At ambient pressure and low temperature, one can expect a phase transformation from the metastable hP12 phase to the DFT ground state hP6 phase, likely via nucleation and growth. However, due to the vanishingly small diffusivity at low temperatures, such a phase transformation is unlikely. Moreover, with the accuracy of the existing exchange-correlation functional, the difference in energy is too small to resolve the question of the ‘true’ low-temperature ground state^{16–19}. Even if the DFT prediction of metastability of 16 meV/atom were correct, we expect the hP12 phase to remain sufficiently metastable.

The hP12 and hR6 structures both have equal number of planar and buckled B layers in their respective unit cells and are related by changes in stacking sequences of W planes along the c axis. If the stacking sequence of W atoms in hP12 is labeled as “AA-BB-AA-BB” then the stacking sequence in hR6 is “AA-BB-CC-AA-BB-CC”. This is also evidenced by the nature of the enthalpy vs pressure curves of the two phases. With increasing pressure, the stability of the hP12 structure increases. From Fig. 2f, the hP6 phase has no planar boron layers. Empirically, the lack of planar B layers might be responsible for the

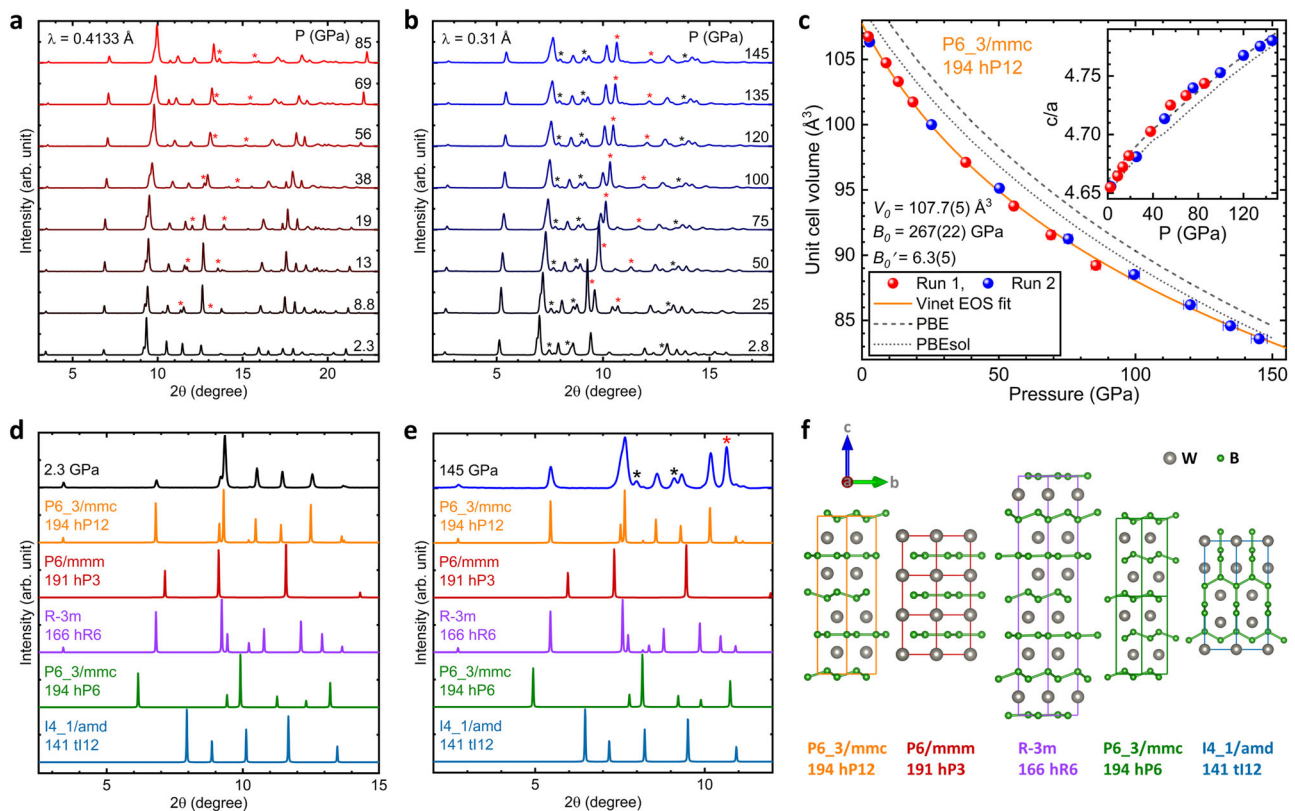


Fig. 2 | High-pressure XRD patterns, PV-isotherm, and crystal structure comparison. **a, b** High-pressure XRD patterns of WB_2 obtained from Runs 1 and 2, respectively, at room temperature using Ne as the quasi-hydrostatic pressure medium. No structural transition was observed throughout the pressure range studied. The star symbols denote the Bragg peaks of the Re gasket (black color) and the Ne pressure-transmitting medium (red color), respectively. **c** The resulting pressure–volume (P–V) curve fitted with the Vinet equation of state (EOS)⁴⁶. The

dashed and dotted lines refer to theoretical calculations from PBE and PBEsol, respectively⁴². The inset shows the c/a ratio versus pressure. **d, e** Comparison of experimental XRD patterns and those of the theoretical structure models from Fig. 3 at 2.3 and 145 GPa. **f** Comparison of crystal structures showing different sequences along the c axis. To aid comparison, the colors of the curves in (**d, e**) match those in the corresponding structure diagrams shown in (**f**).

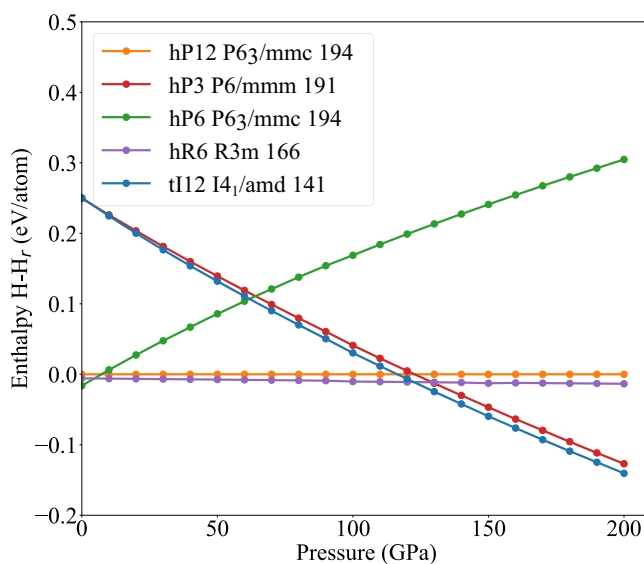


Fig. 3 | Enthalpy of various competing phases of WB_2 as a function of pressure. The hP6 phase of WB_2 has the lowest enthalpy at ambient pressure, and the enthalpies of hP12 and hR6 structures are higher only 16 and 7 meV/atom, respectively.

increasing enthalpy of the hP6 phase with pressure. The tI12 phase consists of B layers with a 90° twist at every $c/4$ increment along the c axis. In contrast to the hP6 phase, the hP3 phase has only planar B layers. Above ~ 130 GPa one can expect the phase transition hP12 \rightarrow hP3, but kinetic barriers may prevent this phase transition.

To investigate the origin of pressure-induced superconductivity in this material, we performed electron–phonon calculations under pressure to determine the theoretical electron–phonon superconducting critical temperature for the hP3, hP12, and hR6 phases. Table 1 summarizes the electron–phonon coupling strength λ and the frequency moments $\bar{\omega}_2$ and ω_{\log} obtained from the Quantum Espresso code. Using the Allen–Dynes equation with $\mu^* = 0.13$, or the formula by Xie et al.²⁰, we find that while both the hR6 and the hP12 structure have consistently subkelvin T_c 's up to 140 GPa, the hP3 structure has a critical temperature of 30 K, relatively insensitive to pressure up to 140 GPa. If experimental lattice constants are used (same a value but four times smaller c in hP12 at 145 GPa), this critical temperature is found to be lower, about 20 K. Details are presented in “Methods”.

It is difficult at first sight to reconcile these results with our data. A structural transition from hP12 to hP3 around 50 GPa would be qualitatively consistent with the T_c data, but there are no clear signatures of hP3 lines in the XRD analysis at any pressure. Furthermore, the theoretical enthalpy difference between hP12 and hP3 phases around 50 GPa is too large to allow the hP12 \rightarrow hP3 bulk phase transformation. Calculations of the density of states near the Fermi surface and the electron–phonon coupling in the hP12 state, on the other hand, show no dramatic changes with pressure, and cannot explain the jump in T_c at 70 GPa with this structure alone.

Table 1 | Pressure (P in GPa), the ω_{\log} and $\bar{\omega}_2$ moments of the spectral function $\alpha^2F(\omega)$ in units of meV and the predicted superconducting transition temperature T_c using the Allen–Dynes equation⁴⁷, isotropic Eliashberg, and the machine-learning equation by Xie et al.²⁰ with $\mu^* = 0.13$

Phase	P	λ	ω_{\log} (meV)	$\bar{\omega}_2$ (meV)	T_c^{AD}	T_c^{El}	T_c^{Xie} (K)
hP12	0	0.37	30.3	47.2	0.4	–	0.4
hP12	100	0.29	41.5	63.6	0	–	0
hP3	100	1.72	17.3	35.5	27.8	27.3	34.5
hR6	0	0.53	27.2	43.2	3.1	–	2.8
hR6	100	0.38	40.4	61.8	0.66	–	0.6

Discussion

In their discovery of superconductivity in MoB₂, Pei et al.⁵ stress that their theoretical calculations indicate important roles for both the Mo d-electrons and for the phonon modes of the Mo. By contrast, in MgB₂ B phonons dominate the electron–phonon coupling strength²¹. Under pressure, Pei et al.⁵ find that the low-pressure β structure of MoB₂ (hR6, space group 166, R $\bar{3}m$, structure prototype CaSi₂) transforms to the high-pressure α MoB₂ (hP3, space group 191, P6/mmm, structure prototype AlB₂) structure, i.e., the same structure as MgB₂.

For WB₂, Fig. 2d shows the experimental XRD pattern in compared with those calculated theoretically for structures relaxed using DFT with PBEsol functional. At high pressures, the peaks from the competing phases line up at certain angles, making it difficult to determine the correct phase from the XRD peaks alone. The most likely crystal structure at high pressures can be inferred by combining information from Figs. 3 and 2, and the theoretically calculated superconducting critical temperatures of various competing phases at high pressure. The tI12 and hP6 structures of WB₂ can be eliminated as the most likely structures at high pressure, since both tI12 and hP6 structures have high theoretical enthalpy, and the XRD peaks of both tI12 and hP6 do not match the experimentally observed peaks.

As further evidence of a lack of bulk structural phase transition in our samples, the electrical resistivity curves of our sample shown in Fig. 1c initially decrease monotonically with pressure and show no clear signature of structural transformation. Because the DOS and electron–phonon coupling show no specific features occurring at or near 50 GPa, we believe that the initial decrease can be attributed to a hardening of the phonon spectrum which reduces the scattering phase space, together with a weak reduction of the electronic DOS with pressure. Both of these effects are indeed seen in our calculations. The minimum must therefore occur because of a relatively rapid increase in scattering in the sample around 50 GPa, of unknown origin.

The same resistivity argument can also help rule out the bulk structural transition to the hR6 phase. In the high-pressure XRD, some of the peaks corresponding to the hR6 phase are missing. For example, at 145 GPa the theoretical peaks of the hR6 phase at $\approx 8.8^\circ$ (i.e., peak by (10 $\bar{1}$ 5) plane) and $\approx 9.9^\circ$ (i.e. peak by (10 $\bar{1}$ 7) plane) are missing from the experimentally measured peaks. Can a strained hR6 lattice produce the experimentally measured peaks? To answer this question we artificially strain the “a” lattice parameter of our DFT relaxed structure and calculate the XRD pattern. The “a” lattice parameter was strained by $\pm 7\%$ in steps of 2% as compared to the relaxed structure. The “c” lattice parameter of our structure was kept unchanged as the XRD peaks that have contributions only by the planes along the “c” direction of the hR6 phase line up almost perfectly with the experimentally measured peaks. Supplementary Figs. 1 and 2 show the theoretical and experimental XRD peaks of the strained hR6 phase at 85 and 145 GPa. The peaks of the strained hR6 structures fail to produce a diffraction pattern that is in agreement with the one measured experimentally. Even if the hR6 phase is present in our sample at high pressures it could be well below the detection limit of the XRD apparatus. Can the

presence of a very small amount of the hR6 phase, undetectable by XRD, account for the superconductivity seen in our samples at high pressure? From the calculated critical temperature in Table 1, high-pressure superconductivity deriving from the hR6 phase is not a credible explanation.

We, therefore, propose that the superconductivity onset at 55 GPa in our samples is due to a filamentary phase formed from stacking faults known to occur in this system⁶. Since our calculations show that the MgB₂-like hP3 phase has a high critical temperature, it appears likely that as the material is plastically deformed with increasing pressure, stacking faults and twin boundaries form. This scenario is further supported by the metastable superconducting behavior of WB₂ during decompression (see Fig. 1d). As discussed below, the structure of these defects can resemble either the structure of the hR6 or hP3 phase locally. A scenario that is consistent with all of the computational and experimental evidence is that the concentration of hP3 defects increases sharply at around 50 GPa, leading to a rise in the resistivity, and, eventually, a percolating path for superconductivity formed around these defects.

Defects of the hR6-type structure in the ambient pressure polycrystalline sample of ref. 6 may also explain the observation of a T_c of a few K. It is interesting to note that when the grains of the samples fabricated in that work decreased in size, superconductivity disappeared. This is consistent with the ease with which defects can migrate to a grain boundary in smaller crystallites. It also suggests that our single-crystal sample contains many fewer stacking faults at ambient pressure, such that defect-induced superconductivity does not occur.

Supplementary Figs. 3 and 4 show how stacking fault and twin boundary defects can be formed in the hP12 phase by sliding appropriate planes. With the introduction of stacking faults and twin boundaries in the hP12 phase, the local environment at the defects can become similar to the hP3 phase.

Figure 4a, h shows the hP3 region formed because of stacking faults and twin boundaries, respectively. Figure 4i shows the calculated stacking fault and twin boundary energy, given by

$$FE_D = \frac{H_D - (N_D * H_{hP12})}{A}, \quad (1)$$

where FE_D is the formation energy of the defect, H_D is the enthalpy of the defect structure, N_D are the number of atoms in the defect structure simulation cell, H_{hP12} is the enthalpy of the hP12 phase and A is the area. The VASP DFT code with PBEsol functional for exchange correlation was used to calculate the enthalpy of the defect structures. A k-point density of 60/Å and a cutoff energy of 520 eV for the plane wave basis set were used in the calculation. The simulation cell used for both defects were made out of 4 hP12 unit cells stacked on top of each other. Both the stacking fault and twin boundary energy decrease as pressure increases, enhancing the probability of formation of these defects. Figure 4b, c shows the density of states (DOS) projected onto the atoms in the hP12 and the hP3 regions of the stacking fault defect structure calculated at 50 GPa. These spatially projected DOS closely match the DOS of the pure bulk hP12 and hP3 phases, respectively. From Figs. 4a–h, it is clear that both the atomic and electronic structures of the stacking fault match those of the pure high- T_c hP3 phase. Similar correlations can also be seen between the projected DOS of the twin boundary (Fig. 4f, g) and that of the pure phases. Both the structural and electronic similarity between the atoms at the planar defect structures and the pure hP3 phase strongly point towards the possibility of superconductivity because of these planar defects. Figure 4j shows the theoretical c/a ratio of the stacking fault and twin boundary defect structures compared to that of a perfect hP12 structure. Thus, one might expect that at a

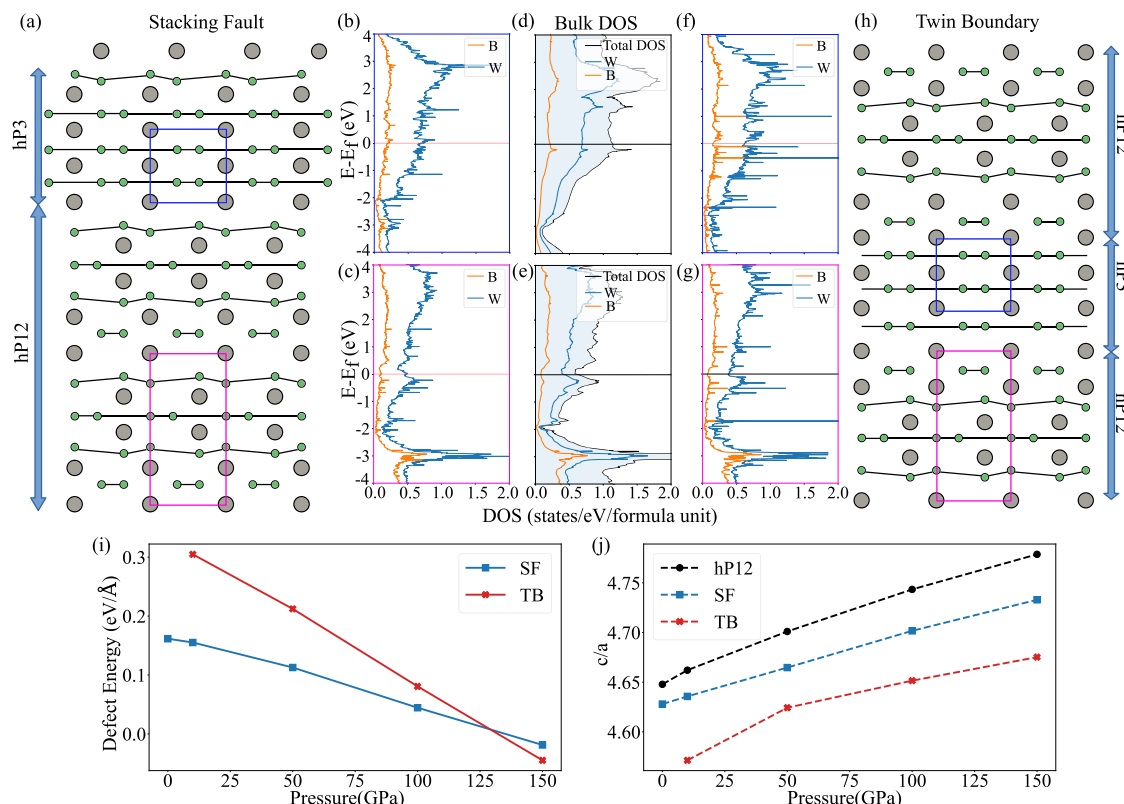


Fig. 4 | Summary of pressure dependent properties of stacking faults and twin boundaries in WB_2 . **a** Stacking faults and **h** twin boundaries in the hP12 phase; the stacking of atomic planes along the c axis at the defect mirrors the stacking in the hP3 phase. Green and gray circles represent boron and tungsten, respectively. **b, c, f, g** projected DOS for the stacking faults and twin boundary. The DOS was spatially projected on the hP3 and hP12 parts of the defect structures. **d, e** DOS of

the bulk hP3 and hP12 phases. All the DOS were calculated at 50 GPa in VASP with PBEsol for exchange-correlation energy. **i** Stacking fault, and twin boundary energy for the hP12 phase as a function of pressure. **j** Theoretical c/a ratio for the hP12 phase with planar defects as a function of pressure. The red curve (crosses) and the blue curve (squares) represent the twin boundary (TB) and the stacking faults (SF), respectively.

given pressure, the introduction of planar defects in the hP12 phase will cause the c/a ratio to decrease. Unfortunately, such a reduction might be below the resolution of XRD apparatus to be observed experimentally and as shown in Fig. 2 the theoretical c/a ratio of the hP12 phase and the experimental c/a ratio match quite well.

Figure 4j shows the theoretical c/a ratio of the hP12 phase with stacking fault and twin boundary defects compared to that of a perfect hP12 structure. Thus, at a given pressure the introduction of planar defects in the hP12 phase should cause the c/a ratio to decrease. Just such a reduction in the c/a ratio at ~60 GPa from its low-pressure extrapolated values is also observed experimentally in the inset of Fig. 2c, providing further evidence for the formation of planar defects with increasing pressure.

In summary, we measured the resistive transition of WB_2 crystals under pressure up to 187 GPa, and shown that superconductivity around 17 K begins near 80 GPa, and that this evolution takes place without a bulk structural transition in the sample. According to X-ray analysis, the system remains nearly entirely in the same bulk crystal structure as at ambient pressure through the onset of T_c . None of the other competing bulk crystal structures are close enough in enthalpy to form, nor do they appear in the XRD patterns. The results lead to the fascinating and plausible scenario in which defects that resemble the hP3 MgB_2 structure locally carry the superconductivity, but are present in filamentary quantities only. This appears to be a novel way to create superconductivity under pressure, and may point to a path to lower the critical pressure of high- T_c superconductors like the hydrides currently under intense investigation.

Methods

Boron pieces (99.98% pure) were wrapped in 99.9% pure tungsten sheet in stoichiometric amounts and arc-melted together. Despite the high melting point (2400 °C) of WB_2 , the low vapor pressures of both B and W at this temperature led to negligible mass loss upon melting the constituents together and remelting twice. Upon cooling, the arc-melted bead showed hexagonal crystal facets on the surface (see Fig. 2d), pieces of which were harvested for the high-pressure measurements. For an example of this method of single-crystal production, see ref. 22.

High-pressure methods

High-pressure X-ray diffraction measurements were performed on a powdered piece of a single-crystal facet from the arc-melted button of WB_2 at Argonne National Laboratory's Advanced Photon Source, beamline 16-BM-D. The X-ray beam had a wavelength of 0.41 Å (30 keV) in Run 1 and 0.31 Å (40 keV) in Run 2, respectively. The X-ray beam was focused to a ~5 μm by 5 μm (FWHM) spot at the sample. An MAR345 image plate detector was used to record the diffracted intensity. Exposure times were typically ~60 to 120 s per image. A CeO_2 standard was used to calibrate the sample to detector distance. Neon was used as the pressure medium. The pressure was determined both using an online ruby fluorescence measurement as well as the equation of state of Au grains loaded into the sample chamber. DIOPTAS²³ software was used to convert the 2D diffraction images to 1D diffraction patterns. The resulting XRD patterns were then further analyzed by Rietveld²⁴ or Le Bail²⁵ methods using GSAS-II software²⁶. The visualization of the crystal structure was depicted using VESTA software²⁷.

For the high-pressure resistivity measurements, a micron-sized WB_2 single-crystal sample ($\sim 40 \times 40 \times 10 \mu\text{m}^3$) was placed in a gas-membrane-driven diamond anvil cell (OmniDAC from Almax-EasyLab) along with a ruby ($\sim 20 \mu\text{m}$ in diameter) for pressure calibration²⁸ below 100 GPa, above which diamond anvil Raman was used²⁹ at -10 K. Pressure was determined via automatic real-time fitting of the ruby spectrum, allowing dense sampling of resistance versus pressure, as the load was smoothly adjusted using a Pace 5000 computer-controlled pressure regulator. Two opposing diamond anvils (type Ia, 1/6-carat, 0.15 mm central flats) were used. A Re metal gasket was pre-indented from -250 to $26 \mu\text{m}$ in thickness with a hole ($\sim 140 \mu\text{m}$ in diameter), which was filled with a 4:1 cBN-epoxy mixture and soapstone (relatively soft) for outer and inner areas, respectively, to electrically insulate the sample from the metal gasket and also serving as the pressure-transmitting medium (see insets in Fig. 1c). The thin WB_2 sample was then placed on top of four thin and pointy Pt leads ($\sim 4 \mu\text{m}$ thick), which were extended by other four longer Pt leads, for a four-point dc electrical resistivity measurement. Further details of the nonhydrostatic high-pressure resistivity technique are given in a paper by Matsuoka et al.³⁰

The diamond cell was placed inside a customized continuous-flow cryostat (Oxford Instruments). A home-built optical system attached to the bottom of the cryostat was used for the visual observation of the sample and for the measurement of the ruby manometer. The pressure was applied at room temperature to the desired pressure, and then the sample was cooled down to -1.8 K and warmed up to room temperature at a rate of -0.25 K/min at each pressure for the temperature-dependent resistivity measurement. To estimate the electrical resistivity from the resistance, we used the van der Pauw method, (assuming an isotropic sample in the measurement plane), $\rho = \pi t R / \ln 2$, where t is the sample thickness ($\sim 10 \mu\text{m}$) with currents of 0.1 – 1 mA. The accuracy of the estimated resistivity is roughly a factor of two or three considering uncertainties in the initial thickness of the sample. No attempt was made to take into account the changes in the sample thickness under high pressures. For the upper critical field measurements, we used a Quantum Design physical property measurement system (PPMS) and an Almax-EasyLab Chicago Diamond Anvil Cell (Chicago-DAC) with two opposing diamond anvils (0.15 and 0.5 mm central flats), whose ruby pressure was measured at room temperature and estimated for the small change in pressure at -10 K. One of the diamonds was a designer-diamond anvil (0.15 mm central flat) with six symmetrically deposited tungsten microprobes in the encapsulated high-quality-homoepitaxial diamond³¹.

Computational methods

To investigate possible phase transitions, at high pressure, we calculated the enthalpy as a function of pressure for the various competing phases of WB_2 . The structures of competing phases were obtained from ref. 12, who investigated the crystal structures of WB_2 up to 200 GPa using the particle swarm optimization algorithm. We used VASP^{32,33} with the PBEsol functional³⁴ for the exchange-correlation energy³⁵ along with the projector augmented wave (PAW) pseudopotentials³⁶ for structural relaxation. A plane wave cutoff of 520 eV and a k-point density of $60/\text{\AA}$ are used in the calculation. The Methfessel–Paxton method was used for smearing the electrons near the Fermi level with a smearing value of 0.1 eV³⁷. For the DOS calculations, we used the tetrahedron method with Blöchl correction³⁸.

Electron–phonon coupling calculations for several phases of WB_2 are carried out using the linear response method as implemented in the Quantum Espresso code^{39–41}. The exchange–correlation potential is chosen to be PBE⁴², and we have used the optimized norm-conserving

pseudopotential^{43,44}. The wave function cutoff is set to 60 Ry and the charge density cutoff is fixed at 240 Ry. For the hP12 and hR6 phases, the k-mesh consists of $16 \times 16 \times 16$ points in the whole Brillouin zone to preserve crystal symmetry, and the q-mesh is $4 \times 4 \times 4$. Brillouin zone integration was carried out using the optimized tetrahedron method⁴⁵. For the hP3 (AlB₂) phase, we first calculate the phonon dispersion on coarse k and q-meshes with $18 \times 18 \times 18$ and $6 \times 6 \times 6$ points, respectively, which are later interpolated onto fine k and q-meshes with $60 \times 60 \times 60$ and $30 \times 30 \times 30$ points, respectively. Isotropic Eliashberg equations are solved to obtain the transition temperatures of the hP3 (AlB₂) phase under pressure.

Data availability

The datasets generated and/or analyzed during this study are available from the corresponding author on reasonable request.

References

- Tomita, T., Hamlin, J. J., Schilling, J. S., Hinks, D. G. & Jorgensen, J. D. Dependence of T_c on hydrostatic pressure in superconducting MgB_2 . *Phys. Rev. B* **64**, 092,505 (2001).
- Deemyad, S. et al. Dependence of the superconducting transition temperature of single and polycrystalline MgB_2 on hydrostatic pressure. *Physica C: Superconductivity* **385**, 105–116 (2003).
- Buza, C. & Yamashita, T. Review of the superconducting properties of MgB_2 . *Superconductor Sci. Technol.* **14**, R115–R146 (2001).
- Bud'ko, S. L. & Canfield, P. C. Superconductivity of magnesium diboride. *Physica C: Superconductivity Appl.* **514**, 142–151 (2015).
- Pei, C. et al. Pressure-induced superconductivity at 32 K in MoB_2 . Preprint at <https://arxiv.org/abs/2105.13250> (2021).
- Kayhan, M. et al. Neutron diffraction and observation of superconductivity for tungsten borides, WB and W_2B_4 . *Solid State Sci.* **14**, 1656–1659 (2012). **The 17th International Symposium on Boron, Borides and Related Materials.**
- Frotscher, M. et al. M_2B_5 or M_2B_4 ? A reinvestigation of the Mo/B and W/B System. *Zeitschrift für anorganische und allgemeine Chemie* **633**, 2626–2630 (2007).
- Khlyustikov, I. & Buzdin, A. Localized superconductivity of twin metal crystals. *Soviet Physics Uspekhi* **31**, 409–433 (1988).
- Drozdov, A. P., Eremets, M. I., Troyan, I. A., Ksenofontov, V. & Shylin, S. I. Conventional superconductivity at 203 kelvin at high pressures in the sulfur hydride system. *Nature* **525**, 73–76 (2015).
- Somayazulu, M. et al. Evidence for superconductivity above 260 K in lanthanum superhydride at megabar pressures. *Phys. Rev. Lett.* **122**, 027,001 (2019).
- Boeri, L. et al. The 2021 room-temperature superconductivity roadmap. *J. Phys.: Condensed Matter* <https://doi.org/10.1088/1361-648x/ac2864> (2021).
- Zhang, K. et al. Superconducting phase induced by a local structure transition in amorphous Sb_2Se_3 under high pressure. *Phys. Rev. Lett.* **127**, 127,002 (2021).
- Wang, C. et al. WB_2 : not a superhard material for strong polarization character of interlayer W-B bonding. *Phys. Chem. Chem. Phys.* **19**, 8919–8924 (2017).
- Hennig, R. G. et al. Phase transformation in Si from semiconducting diamond to metallic β -Sn phase in QMC and DFT under hydrostatic and anisotropic stress. *Phys. Rev. B* **82**, 014,101 (2010).
- Yin, S. et al. Hardness and elastic moduli of high pressure synthesized MoB_2 and WB_2 compacts. *High Pressure Res.* **33**, 409–417 (2013).
- Zhang, Y. et al. Efficient first-principles prediction of solid stability: towards chemical accuracy. *npj Comput. Mater.* **4**. <https://doi.org/10.1038/s41524-018-0065-z> (2018).

17. Yang, J. H., Kitchaev, D. A. & Ceder, G. Rationalizing accurate structure prediction in the meta-GGA SCAN functional. *Phys. Rev. B* **100** <https://doi.org/10.1103/physrevb.100.035132> (2019).
18. Hinuma, Y., Hayashi, H., Kumagai, Y., Tanaka, I. & Oba, F. Comparison of approximations in density functional theory calculations: energetics and structure of binary oxides. *Phys. Rev. B* **96** <https://doi.org/10.1103/physrevb.96.094102> (2017).
19. Bartel, C. J., Weimer, A. W., Lany, S., Musgrave, C. B. & Holder, A. M. The role of decomposition reactions in assessing first-principles predictions of solid stability. *npj Comput. Mater.* **5** <https://doi.org/10.1038/s41524-018-0143-2> (2019).
20. Xie, S.R. et al. Machine learning of superconducting critical temperature from Hliahberg theory. *npj Comput. Mater.* **8** <https://doi.org/10.1038/s41524-021-00666-7> (2022).
21. Mazin, I. & Antropov, V. Electronic structure, electron-phonon coupling, and multiband effects in MgB₂. *Physica C: Superconductivity* **385**, 49–65 (2003).
22. Heuser, K., Scheidt, E. W., Schreiner, T., Fisk, Z. & Stewart, G. Low temperature specific heat of CeRu₂Si₂ at the field induced metamagnetic instability. *J. Low Temp. Phys.* **118**, 235–239 (2000).
23. Prescher, C. & Prakapenka, V. B. Dioptas: a program for reduction of two-dimensional X-ray diffraction data and data exploration. *High Pressure Res.* **35**, 223–230 (2015).
24. Rietveld, H. M. A profile refinement method for nuclear and magnetic structures. *J. Appl. Crystallography* **2**, 65–71 (1969).
25. Le Bail, A., Duroy, H. & Fourquet, J. Ab-initio structure determination of LiSbWO₆ by X-ray powder diffraction. *Mater. Res. Bull.* **23**, 447–452 (1988).
26. Toby, B. H. & Von Dreele, R. B. GSAS-II: the genesis of a modern open-source all purpose crystallography software package. *J. Appl. Crystallography* **46**, 544–549 (2013).
27. Momma, K. & Izumi, F. VESTA: a three-dimensional visualization system for electronic and structural analysis. *J. Appl. Crystallography* **41**, 653–658 (2008).
28. Chijioke, A. D., Nellis, W. J., Soldatov, A. & Silvera, I. F. The ruby pressure standard to 150 GPa. *J. Appl. Phys.* **98**, 114,905 (2005).
29. Akahama, Y. & Kawamura, H. Pressure calibration of diamond anvil Raman gauge to 310 GPa. *J. Appl. Phys.* **100**, 043,516 (2006).
30. Matsuoka, T. & Shimizu, K. Direct observation of a pressure-induced metal-to-semiconductor transition in lithium. *Nature* **458**, 186–189 (2009).
31. Weir, S. T., Akella, J., Aracne-Ruddle, C., Vohra, Y. K. & Catledge, S. A. Epitaxial diamond encapsulation of metal microprobes for high pressure experiments. *Appl. Phys. Lett.* **77**, 3400–3402 (2000).
32. Kresse, G. & Furthmüller, J. Efficiency of ab-initio total energy calculations for metals and semiconductors using a plane-wave basis set. *Comput. Mater. Sci.* **6**, 15–50 (1996).
33. Kresse, G. & Furthmüller, J. Efficient iterative schemes for ab initio total-energy calculations using a plane-wave basis set. *Phys. Rev. B* **54**, 11,169–11,186 (1996).
34. Csonka, G. I. et al. Assessing the performance of recent density functionals for bulk solids. *Phys. Rev. B* **79** <https://doi.org/10.1103/physrevb.79.155107> (2009).
35. Perdew, J. P. et al. Restoring the density-gradient expansion for exchange in solids and surfaces. *Phys. Rev. Lett.* **100** <https://doi.org/10.1103/physrevlett.100.136406> (2008).
36. Blöchl, P. E. Projector augmented-wave method. *Phys. Rev. B* **50**, 17,953–17,979 (1994).
37. Methfessel, M. & Paxton, A. T. High-precision sampling for Brillouin-zone integration in metals. *Phys. Rev. B* **40**, 3616–3621 (1989).
38. Blöchl, P. E., Jepsen, O. & Andersen, O. K. Improved tetrahedron method for Brillouin-zone integrations. *Phys. Rev. B* **49**, 16,223–16,233 (1994).
39. Giannozzi, P. et al. QUANTUM ESPRESSO: a modular and open-source software project for quantum simulations of materials. *J. Phys.: Condensed Matter* **21**, 395,502 (2009).
40. Giannozzi, P. et al. Quantum espresso toward the exascale. *J. Chemical Phys.* **152**, 154,105 (2020).
41. Giannozzi, P. et al. Advanced capabilities for materials modelling with quantum ESPRESSO. *J. Phys.: Condensed Matter* **29**, 465,901 (2017).
42. Perdew, J. P., Burke, K. & Ernzerhof, M. Generalized gradient approximation made simple. *Phys. Rev. Lett.* **77**, 3865–3868 (1996).
43. Hamann, D. R. Optimized norm-conserving Vanderbilt pseudopotentials. *Phys. Rev. B* **88** <https://doi.org/10.1103/physrevb.88.085117> (2013).
44. Schlipf, M. & Gygi, F. Optimization algorithm for the generation of ONCV pseudopotentials. *Computer Phys. Commun.* **196**, 36–44 (2015).
45. Kawamura, M., Gohda, Y. & Tsuneyuki, S. Improved tetrahedron method for the Brillouin-zone integration applicable to response functions. *Phys. Rev. B* **89**, 094,515 (2014).
46. Vinet, P., Ferrante, J., Rose, J. H. & Smith, J. R. Compressibility of solids. *J. Geophys. Res.: Solid Earth* **92**, 9319–9325 (1987).
47. Allen, P. B. & Dynes, R. C. Transition temperature of strong-coupled superconductors reanalyzed. *Phys. Rev. B* **12**, 905–922 (1975).

Acknowledgements

Work at the University of Florida performed under the auspices of U.S. Department of Energy Basic Energy Sciences under Contract No. DE-SC-0020385. We thank S. Tkachev (GSECARS, University of Chicago) for sample gas loading for the x-ray diffraction measurements. We acknowledge Curtis Kenny Benson, HPCAT, for technical assistance. A.C.H. and R.G.H. acknowledge support from the National Science Foundation under award PHY-1549132 (Center for Bright Beams) and award DMR-2118718. Y.K.V. acknowledges the support from DOE-NNSA award DE-NA0003916. R.S.K. and R.J.H. acknowledge support from the U.S. National Science Foundation (DMR-1933622 and DMR-2119308). X-ray diffraction measurements were performed at HPCAT (Sector 16), Advanced Photon Source (APS), Argonne National Laboratory. HPCAT operations are supported by the DOE-National Nuclear Security Administration (NNSA) Office of Experimental Sciences. The beamtime was made possible by the Chicago/DOE Alliance Center (CDAC), which is supported by DOE-NNSA (DE-NA0003975). Use of the gas loading system was supported by COMPRES under NSF Cooperative Agreement EAR-1606856 and by GSECARS through NSF grant EAR-1634415 and DOE grant DE-FG02-94ER14466. The Advanced Photon Source is a DOE Office of Science User Facility operated for the DOE Office of Science by Argonne National Laboratory under Contract No. DE-AC02-06CH11357. We thank M. Trenary for useful discussions and comments on the manuscript. High-pressure equipment development at the University of Florida was supported by National Science Foundation CAREER award DMR-1453752.

Author contributions

The initial computational T_c estimates that motivated this study were performed by Y.Q. High-pressure electrical resistivity measurements were performed by J.L. with the assistance of S.S. DFT calculations and analysis were performed by A.C.H. with contributions from SRX at an early stage. Samples were synthesized and characterized at ambient pressure by J.S.K. and G.R.S. High-pressure X-ray measurements and analyses were performed by J.L. with the assistance of R.S.K., D.P., C.P., and R.J.H. X-ray data analysis were performed by J.L. and A.C.H. Y.K.V. lead the fabrication of designer-diamond anvils that were used for a portion of the high-pressure electrical resistivity measurements. The paper was written primarily by J.L., A.H., J.J.H., R.G.H., P.J.H., and G.R.S., with contributions and comments from the other authors. The study was conceived and organized by J.J.H., R.G.H., P.J.H., and G.R.S.

Competing interests

The authors declare no competing interests.

Additional information

Supplementary information The online version contains supplementary material available at <https://doi.org/10.1038/s41467-022-35191-8>.

Correspondence and requests for materials should be addressed to J. J. Hamlin.

Reprints and permissions information is available at <http://www.nature.com/reprints>

Publisher's note Springer Nature remains neutral with regard to jurisdictional claims in published maps and institutional affiliations.

Open Access This article is licensed under a Creative Commons Attribution 4.0 International License, which permits use, sharing, adaptation, distribution and reproduction in any medium or format, as long as you give appropriate credit to the original author(s) and the source, provide a link to the Creative Commons license, and indicate if changes were made. The images or other third party material in this article are included in the article's Creative Commons license, unless indicated otherwise in a credit line to the material. If material is not included in the article's Creative Commons license and your intended use is not permitted by statutory regulation or exceeds the permitted use, you will need to obtain permission directly from the copyright holder. To view a copy of this license, visit <http://creativecommons.org/licenses/by/4.0/>.

© The Author(s) 2022